Magnetic resonance velocimetry in high-speed turbulent flows
sources of measurement errors and a new approach for higher accuracy

John, Kristine ; Jahangir, Saad; Gawandalkar, Udhav Ulhas; Hogendoorn, Willian; Poelma, Christian; Grundmann, Sven ; Bruschewski, Martin

DOI
10.1007/s00348-019-2849-4

Publication date
2020

Document Version
Final published version

Published in
Experiments in Fluids

Citation (APA)
John, K., Jahangir, S., Gawandalkar, U. U., Hogendoorn, W., Poelma, C., Grundmann, S., & Bruschewski, M. (2020). Magnetic resonance velocimetry in high-speed turbulent flows: sources of measurement errors and a new approach for higher accuracy. *Experiments in Fluids*, *61*(2), Article 27. https://doi.org/10.1007/s00348-019-2849-4

Experiments in Fluids (2020) 61:27
https://doi.org/10.1007/s00348-019-2849-4

RESEARCH ARTICLE

Magnetic resonance velocimetry in high-speed turbulent flows: sources of measurement errors and a new approach for higher accuracy

Kristine John[1] · Saad Jahangir[2] · Udhav Gawandalkar[2] · Willian Hogendoorn[2] · Christian Poelma[2] · Sven Grundmann[1] · Martin Bruschewski[1]

Received: 7 August 2019 / Revised: 25 October 2019 / Accepted: 11 November 2019

Abstract

This study focuses on the measurement accuracy of Magnetic Resonance Velocimetry (MRV) in high-speed turbulent flows. One of the most prominent errors in MRV is the displacement error, which describes the misregistration of spatial coordinates and velocity components in moving fluids. Displacement errors are particularly critical for experiments with high flow velocity and high spatial resolution. The degree of displacement error also depends on the sequence structure of the MRV technique. In this study, two MRV sequence types are examined regarding their measurement capabilities in high-speed turbulent flows: a conventional MRV sequence based on the popular "4D FLOW" technique, and a newly developed sequence, named "SYNC SPI". Compared to conventional MRV, SYNC SPI is designed for high measurement accuracy, and not for imaging speed, which limits its application to statistically stationary flows. Both sequence types are evaluated in a flow experiment with a converging–diverging nozzle. Time-averaged results are presented for velocities up to 12 m/s at the throat. Supported by Particle Imaging Velocimetry, it is shown that SYNC SPI is capable of acquiring accurate velocity data in these highly turbulent flows. In contrast, the data from the conventional MRV sequence exhibits substantial displacement errors with a maximum displacement of 21 mm. The long acquisition time is the main disadvantage of the SYNC SPI sequence. Therefore, it is examined if undersampling and non-linear reconstruction, known as Compressed Sensing, can be utilized to make data acquisition more efficient. In the presented measurements, Compressed Sensing is successfully applied to shorten the acquisition time by up to 70% with almost no reduction in measurement accuracy.

This work was supported by the Bundesministerium für Wirtschaft und Energie (BMWi) under Grant Number 20E1708 and ERC Consolidator Grant 725183 'OpaqueFlows'.

✉ Martin Bruschewski
martin.bruschewski@uni-rostock.de

Kristine John
kristine.john@uni-rostock.de

[1] Institute of Fluid Mechanics, University of Rostock, Rostock, Germany

[2] Laboratory for Aero and Hydrodynamics, Technische Universiteit Delft, Delft, The Netherlands

Published online: 14 January 2020

Graphic abstract

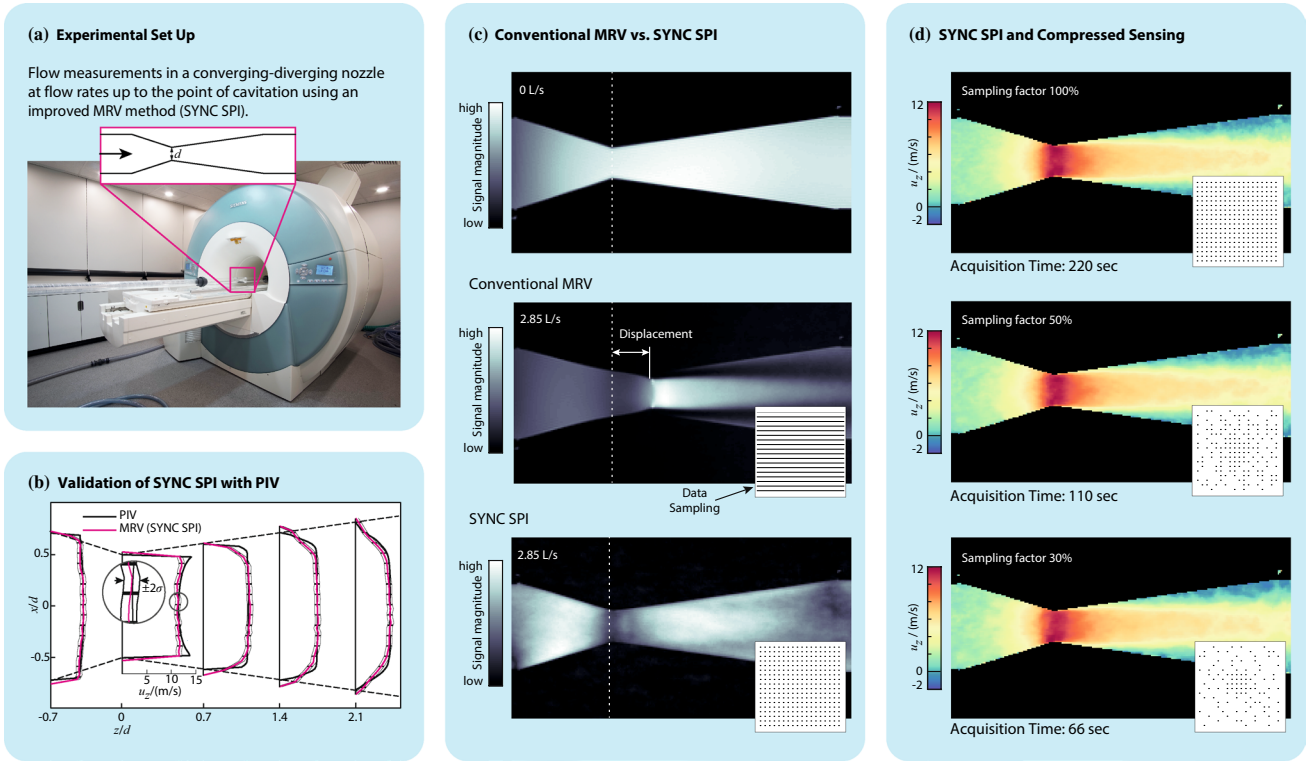

1 Introduction

Magnetic Resonance Velocimetry (MRV) has great potential to become a versatile and economical 3D velocity measurement technique for applied fluid mechanics. Based on medical Magnetic Resonance Imaging (MRI), this measurement technique enables full-field velocity measurements without optical access, and without seeding in highly complex flow systems (Elkins and Alley 2007).

Despite many successful case studies, wide-spread acceptance of MRV for research and development is still hampered by some unaddressed problems. One of the most dominant errors in MRV is the effect of displacement, also known as misregistration (Larson et al. 1990; Nishimura et al. 1991). This error describes the effect of the spatial displacement of the fluid during the encoding of space and velocity. As a result of the fluid motion, the flow velocity components and each spatial coordinate are encoded at different positions in the flow field but are registered for a single position in space, which leads to incorrect data sets. The overall aim of this study is to highlight the significance of displacement errors and to provide an improved technique.

Recently, a new MRV sequence, named SYNC SPI (single point imaging with synchronized encoding) has been developed to reduce these errors to a minimum (Bruschewski et al. 2019). The main disadvantage of SYNC SPI is the relatively long acquisition time, which limits the application of this technique to mean velocity measurements in statistically stationary flows.

This study continues the development of SYNC SPI. A recently developed undersampling technique, known as Compressed Sensing, is used to reduce the number of samples without reducing the measurement resolution. It is shown that the acquisition time can be reduced by 70% while still maintaining high measurement accuracy. Validation with Particle Imaging Velocimetry (PIV) proves the reliability of this approach.

1.1 Mechanism of displacement errors in MRV

As a particular feature of MRI (and MRV), the data is sampled in the spatial-frequency domain, which is commonly termed *k*-space. The Fast Fourier transform (FFT) of the *k*-space data yields a two- (or three-dimensional) image of the measured flow field. Each pixel (or voxel) in this image

contains a complex signal. The phase angle of the signal is typically encoded such that it represents velocity, whereas the signal magnitude typically represents the distribution of hydrogen protons in the Field Of View (FOV). A detailed description of the image reconstruction and velocity encoding process can be found in Elkins and Alley (2007).

The encoding of space and velocity requires a series of magnetic field gradients that are repetitively played out in a sequence. These gradients have a finite duration, and commonly, the timing is different. The finite duration and the timing differences of these gradients are the cause of displacement errors. Two major mechanisms can be identified (Bruschewski et al. 2019):

- *Inter-encoding misregistration* This effect describes the error caused by the fact that each encoding event provides only one velocity component or spatial coordinate, and the fluid moves between events. The timing differences lead to distortions in the flow geometry. The determining parameter for inter-encoding misregistration is the maximum timing difference in the sequence, named encoding delay. The encoding of all coordinates and velocity components must be synchronized to remove this type of error.
- *Intra-encoding misregistration* The second type of displacement error is related to the length of the individual encoding events. The finite encoding durations cause blurring of the measured location and velocity. This effect cannot vanish entirely but can be reduced with shorter encoding times.

In summary, inter-encoding misregistration results in distorted velocity fields, whereas intra-encoding misregistration causes blurring and smearing.

Conventional MRV techniques are typically based on the "4D FLOW" sequence as the by far most commonly used MRI technique for the visualization of medical flows (Markl et al. 2012). Originally, this class of sequences was developed to acquire phase-resolved 3D images of periodic processes in the human body, therefore the name 4D FLOW. Conventionally, 4D FLOW is designed as a gradient-echo sequence with Cartesian encoding. This encoding scheme is known as frequency encoding. Multiple data points along a line in k-space are sampled simultaneously to a readout gradient. As a result, the acquisition time is greatly reduced. The basic layout of this sequence is depicted in Fig. 1a.

The encoding gradients in 4D FLOW are typically combined using the approach in Bernstein et al. (1992) to achieve minimum echo time (TE). Despite the short sequence timing, the readout gradient necessary for frequency encoding leads to unavoidable timing differences in the encoding process. The effect of the timing parameters on the displacement of the signal in a fluid flow is demonstrated below the sequence diagram in Fig. 1a. It can be seen that conventional MRV has a significant encoding delay and relatively long encoding intervals, which promotes inter- and intra-misregistration errors.

For comparison, the new SYNC SPI sequence is depicted in Fig. 1b. Unlike conventional MRV, the k-space is measured point-by-point. Since there is no readout gradient, all space and velocity encoding gradients can be synchronized. As a result, the encoding delay is zero, and, therefore, inter-encoding misregistration is completely removed. The full design strategy behind SYNC SPI and a detailed comparison to conventional MRV and other MRI sequences can be found in Bruschewski et al. (2019).

In the case of conventional MRV, the maximum distortions in the flow field caused by inter-encoding misregistration can be estimated using the encoding delay and the maximum velocity in the flow field. As seen in Fig. 1a, the encoding delay is defined as the time between the center of the first phase-encoding gradient and the center of the frequency-encoding gradient. Velocity encoding is typically applied simultaneously to the phase-encoding gradient or after. The estimation yields:

$$\text{displacement} \approx \text{max. velocity} \times \frac{\text{encoding delay}}{\text{voxel size}} \tag{1}$$

which represents the maximum displacement in the flow field in number of voxels. In some cases, the calculation of the encoding delay is not possible since the detailed timing parameters of the sequence are not always provided. In these cases, the displacement in the flow field can be estimated based on TE, which is a more common timing parameter:

$$\text{displacement} \approx \text{max. velocity} \times \frac{\text{TE}}{\text{voxel size}} \tag{2}$$

As depicted in Fig. 1a, TE is always longer than the actual encoding delay. Therefore, Eq. (2) is considered a more conservative estimator than Eq. (1).

Table 1 provides an overview of displacement errors in selected case studies that applied the 4D FLOW sequence or a similar sequence in laboratory flow experiments. This literature survey covers the typical measurement conditions of MRV in these studies and is therefore considered to be representative. The displacement error in the flow field is estimated with Eqs. (1) and (2). Many studies listed here exhibit a high degree of displacement error. The maximum estimated displacement is 12 or 14.8 voxels, depending on the estimator. These studies would greatly benefit from an MRV technique that is more robust to displacement errors.

It must be stressed that displacement errors depend mainly on the velocity magnitude in the flow, and that this error may occur in any flow measurement regardless of

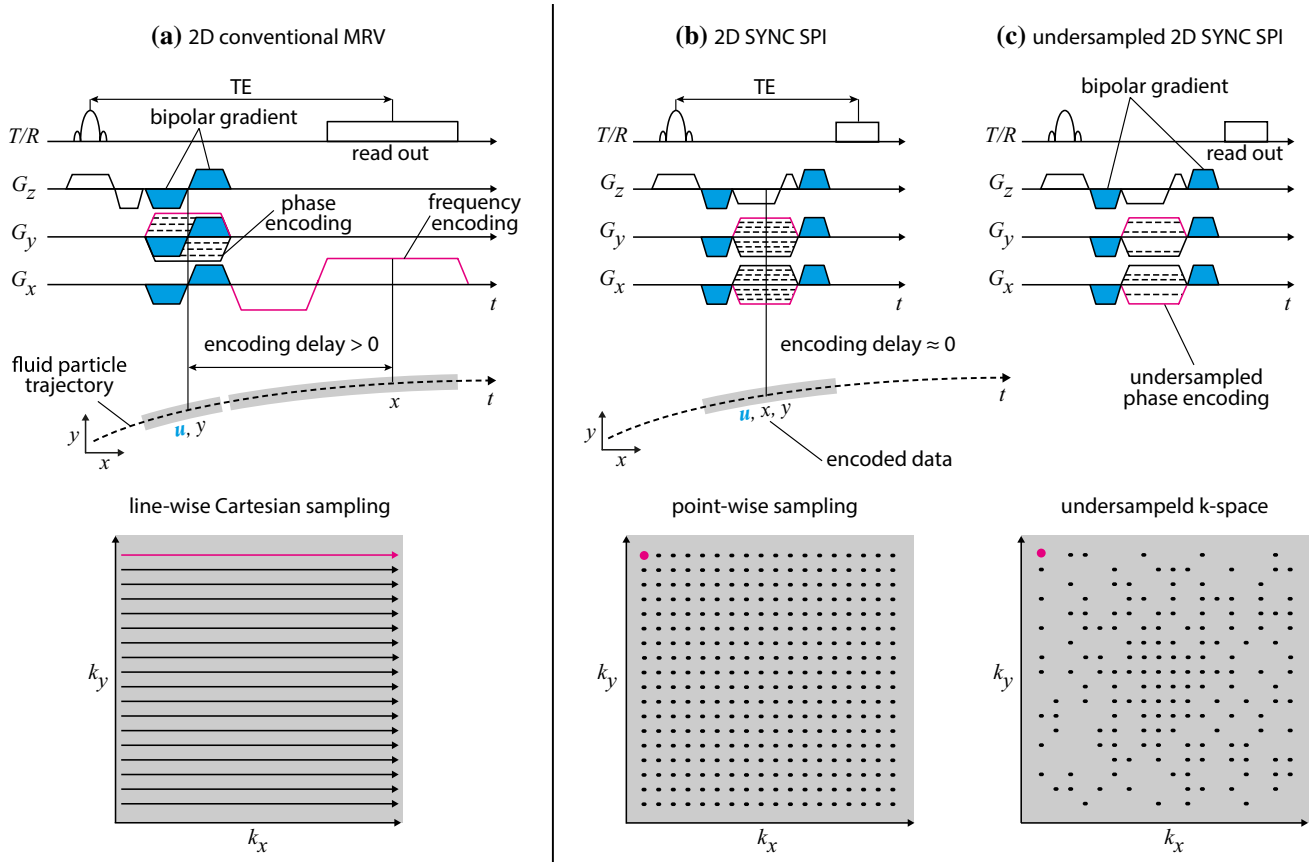

Fig. 1 Schematic sequence diagrams for a conventional MRV sequence (**a**) and the SYNC SPI sequence with regular sampling (**b**) and with undersampling (**c**). Gradient wave forms filled with blue indicate velocity encoding. Gradient wave forms with red contours indicate spatial encoding. The effect of displacement errors and the associated *k*-space sampling patterns are shown below the sequence diagrams

Table 1 Description of previous studies using an MRV sequence based on the 4D FLOW technique

Reference	Characteristic voxel length (mm)	TE (ms)	Encoding delay (ms)	max. velocity (m/s)	Displacement based on encoding delay (number of voxels)	Displacement based on TE (number of voxels)
Elkins et al. (2009)	1.0	2.0	–	1.6	–	3.2
Onstad et al. (2011)	0.6	2.6	–	0.2	–	0.9
Grundmann et al. (2012)	1.0	3.3	2.6	2.2	6.6	7.3
Wassermann et al. (2013)	1.0	3.7	3.0	4.0	12.0	14.8
Freudenhammer et al. (2014)	1.0	4.1	3.3	1.5	5.0	6.2
Piro et al. (2016)	0.8	3.2	2.4	2.0	6.0	8.0
Bruschewski et al. (2016b)	1.0	3.1	2.4	2.3	5.5	7.1
Ching et al. (2018)	0.8	1.8	–	1.1	–	2.5
Baek et al. (2019)	1.0	3.7	–	1.3	–	4.8

The estimated degree of displacement error is quantified by the number of voxels using Eqs. (1) and (2). The characteristic voxel length is the voxel length in the main flow direction. In some cases, the encoding delay could not be determined because the sequence timing was not known

the complexity of the flow system. Particularly for simpler flow systems with fairly uniform flows, these errors might be overlooked because displacement effects are often not directly visible. In any case, displacement errors lead to wrong measurement results.

1.2 Imaging acceleration with compressed sensing

While SYNC SPI is insensitive to inter-encoding displacement errors, the overall acquisition time is relatively long. A novel method to reduce the acquisition time without a significant loss in data quality is Compressed Sensing. This concept was initially developed by Candes et al. (2006) and Donoho (2006). Thereupon, Lustig et al. (2007) demonstrated the application of Compressed Sensing in MRI. Since then, an increasing number of studies investigated the use of Compressed Sensing for medical MRI applications (Untenberger et al. 2016). Applying Compressed Sensing to SYNC SPI appears as a logical step.

Compressed Sensing requires a sparse representation of the measured data. The term sparsity means that the majority of the data points are very close to zero. These data points can be set to zero without a significant loss in data quality. Image and video compression are prominent examples of this concept. In Compressed Sensing, this concept is utilized to reduce the number of samples that are required to measure a signal. Incoherent samples are essential to avoid aliasing errors that arise due to the violation of the Nyquist criterion. After a properly conducted non-linear reconstruction, the data is very close to the fully sampled data, although much fewer samples are acquired.

The principles of Compressed Sensing in MRI can be described as follows. The *k*-space is undersampled with a random pattern to provide incoherent samples. All data points that are not measured are filled with zeros. The design of the sampling pattern includes the prior knowledge that the center of *k*-space normally contains the highest signal density. Therefore, the sampling pattern is often designed so that the sampling probability increases towards the center of the *k*-space (Lustig et al. 2008). As an example, such a sampling pattern is visualized in Fig. 1c.

The randomly distributed samples cause noise-like artifacts in the conventionally (FFT-based) reconstructed image. A non-linear reconstruction similar to the one in Lustig et al. (2007) can be used to reduce these errors and, therefore, recover the sparsely measured object. The reconstruction is realized by minimizing the sparse representation of the reconstructed image X in a transformation domain with the transform operator Ψ:

$$\min \quad ||\Psi X||_1 \tag{3}$$

In this study, Ψ is determined as the Total Variation of the data in the image space. Other transformations are possible such as the Wavelet transform or the discrete cosine transform, which requires significantly more computing time (Holland et al. 2010). The solution of Eq. (3) is restricted by the condition that the spatial frequencies of the reconstructed image need to match the measured *k*-space data Y within a defined tolerance ε:

$$||\mathrm{FT}_s\{X\} - Y||_2 < \varepsilon \tag{4}$$

where FT_s denotes the sparse Fourier transform. Similar to the approach proposed in Lustig et al. (2007), the optimization is solved in its unconstrained Lagrangian form using projected conjugate gradients. In this approach, deviations may arise in the reconstructed image phase in which the velocity information is encoded.

For this reason, suggestions from Holland et al. (2010) are used in this study to achieve an accurate reconstruction of the image phase. For more details on the reconstruction procedure applied in this study, the reader is referred to Lustig et al. (2007) and Holland et al. (2010).

2 Methods

2.1 Sequence design

As mentioned in the Introduction section, the main disadvantage of SYNC SPI is the comparatively long acquisition time. A reduction in acquisition time is here achieved with Compressed Sensing. An implementation of Compressed Sensing in the SYNC SPI sequence is straight-forward since all *k*-space points are independently sampled. Arbitrary undersampling patterns can be easily implemented. For comparison, a fully sampled SYNC SPI and a state-of-the-art conventional MRV sequence based on the well-known 4D FLOW technique are evaluated. The basic sequence structures of all investigated sequences are depicted in Fig. 1. For further details on the sequence design, the reader is referred to Bruschewski et al. (2019).

2.2 Setup of MRV experiments

An axisymmetric converging–diverging nozzle (venturi) with flow velocities up to the point of cavitation was used to investigate the potentials of fully sampled and compressed sensed SYNC SPI. This test case was chosen because the detection of displacement errors in such accelerating and decelerating flow is relatively simple. This venturi geometry is an established benchmark flow. Detailed descriptions are given, for example, by Jahangir et al. (2018).

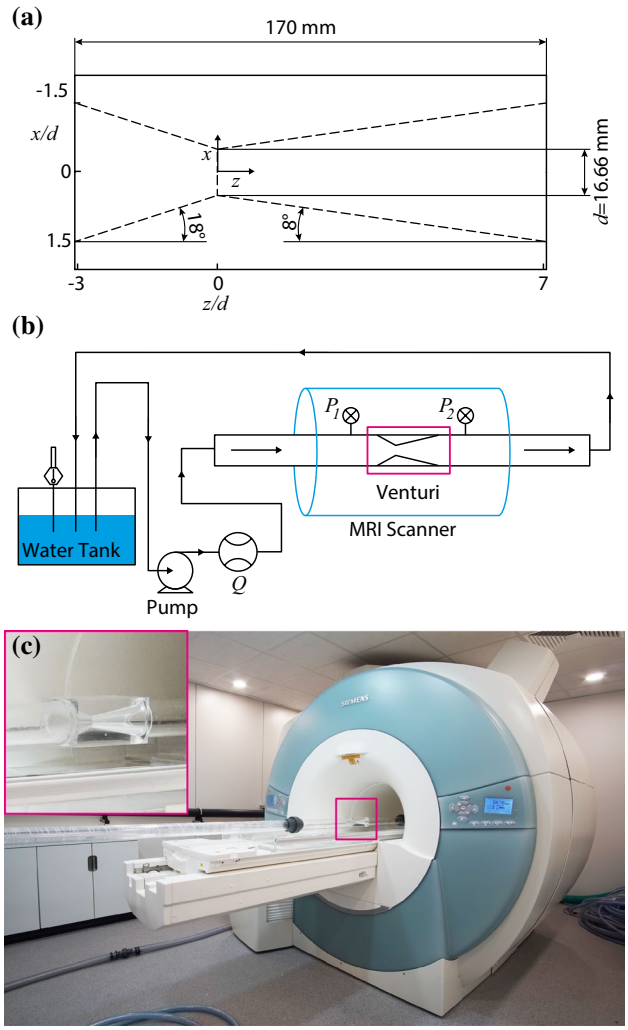

Fig. 2 Design of the venturi (**a**), schematic of the flow loop (**b**), set up of the MRV measurement inside the examination room (**c**)

MRV measurements were performed on a 3 Tesla whole-body Magnetom TRIO (Siemens, Erlangen, Germany) with maximum gradient amplitude of 38 mT/m and a maximum slew rate of 170 T/m/s. The scanner is part of the MRI laboratory at the Institute of Fluid Mechanics at the University of Rostock. Unlike most MRI facilities usually used for medical examination, this laboratory is specially designed for fluid mechanics applications. Two standard multi-channel matrix coils with six channels each were used to receive the signal from FOV. The venturi and the pipes inside the examination room were made from PMMA, as this material matches the magnetic susceptibility of water (Wapler et al. 2014). The design of the venturi, the experimental set-up, and the schematic of the flow loop are depicted in Fig. 2.

The flow medium was purified water with 6 g/L $CuSO_4$ added as a contrast agent to allow high excitation rates at high flip angles. A variable speed pump provided a constant flow rate of 1.38 L/s, 2.35 L/s, and 2.85 L/s, corresponding to a Reynolds number of 35,000, 60,000, and 71,300 based on the pipe diameter of 50 mm. The flow loop was guided through a tank with 700 L of additional fluid to limit the temperature increase of the fluid during the experiment. The flow rate, temperature, and pressure before and after the venturi were monitored during all experiments to verify the stable measurement conditions.

2.3 MRV protocol and post-processing

Table 2 summarizes the measurement parameters of all applied MRV sequences. The conventional MRV sequence based on 4D FLOW was designed to achieve the lowest possible displacement errors for this type of sequence on this specific MRI system. The highest possible receiver

Table 2 Measurement parameters of the applied MRV sequences

	Conventional MRV	SYNC SPI 100% sampled	70%	50%	30%	10%
Matrix size (x,y,z)	(512,1,512)	(128,1,512)				
FOV (mm)	(384,5,384)	(96,5,384)				
Encoding	(PE,SS,FE)	(PE,SS,PE)				
TE (ms)	2.7	1.2				
TR (ms)	4.7	1.7				
BW (kHz)	415	8				
Excitation pulse BWT	8	2				
Flip angle (°)	15	15				
Velocity encoding method	4-point-balanced	2-point (only in z)				
VENC (m/s)	(5,5,5)	(–,–,7.2*/12.6**/16.4***)				
Averages	12	9				
TA (s)	10	220	154	110	66	22

The parameters FE, PE, and SS denote the frequency encoding, phase encoding, and slice-selection direction, respectively. TA is the acquisition time for a single measurement. The VENC in the SYNC SPI sequence was adjusted according to the maximum expected velocities in the three experiments: (*) 1.38 L/s, (**) 2.35 L/s, (***) 2.85 L/s

bandwidth was applied to make the timing of this sequence as short as possible. Furthermore, a slight asymmetry of the echo during readout was accepted, which resulted in a shorter pre-phasing gradient prior to readout and, therefore, shorter timing.

The SYNC SPI sequence was explicitly designed for this study with the sequence prototyping framework pulseq (Layton et al. 2017). The image orientation and the measurement resolution were the same in both sequences. However, because of practical reasons, there were some differences in the protocols. The conventional MRV sequence used in this study restricted the value of VENC to a maximum of 5 m/s. All velocity aliasing errors that occurred due to flow velocities larger than 5 m/s were corrected after the measurement using an algorithm that searched for non-physical velocity gradients. All three velocity components were acquired using the 4-point balanced method. In the case of SYNC SPI, the parameter VENC was adjusted according to the maximum flow velocity, and only the axial flow velocities were encoded. Furthermore, the SYNC SPI protocol was designed to achieve the lowest possible timing to keep the acquisition time as low as possible. For this reason, the bandwidth-time-product (BWT) of the slice excitation pulse was set to the lowest possible value. Also, the FOV was smaller to reduce time. These differences may affect the precision of the data; however, the influence on the key outcomes of this study, which is the sensitivity of the sequence to displacement errors, is considered negligible.

The SYNC SPI data was fully sampled, as depicted in Fig. 1b. The acquired data sets were then resampled with an undersampling mask to achieve data sets with 10%, 30%, 50%, and 70% sampling factor. With this technique, the same data basis was used for all image reconstructions. All differences that arose in the reconstructed images are therefore related to the undersampling and image reconstruction process, and not due to differences in the experimental conditions.

Note that from a statistical point of view, the resampling of a fully sampled SYNC SPI data set with an undersampling mask produces the same data as if the data was undersampled during the measurement. The reason is that each *k*-space point was measured separately in the SYNC SPI sequence. Possible coherence between *k*-space points was removed by RF-spoiling. Distant correlations and stimulated echoes were intrinsically removed because the signal decays within few milliseconds in such highly turbulent flow. These assumptions have been confirmed experimentally. A flow measurement in the venturi was carried out twice, once with an ordered *k*-space scan (point by point along the *k*-spaces axes), and once with a completely random sampling order. Absolutely no systematic differences were observed in the measured data. The order of *k*-space sampling, therefore, has a negligible effect in this measurement. Consequently, the synthetically undersampled *k*-space data should be very close to actual undersampled data.

The undersampled SYNC SPI data sets were zero-filled and non-linear reconstructed using the optimization process described alongside Eqs. (3) and (4). The non-linear reconstruction was performed separately for all velocity encoding points and coil images. Afterward, the signal phase, hence the velocity maps, were obtained from the linear combination of the complex coil data. The image magnitude was reconstructed using the sum-of-squares approach. The same reconstruction was also used for the fully sampled data sets, including the 4D FLOW data.

After reconstruction, measurements with the same sequence settings but without flow were subtracted from all velocity data to compensate eddy current effects caused by the switching of the magnetic field gradients. The measurement uncertainty was estimated using the difference-approach from Bruschewski et al. (2016a). It is stressed that no data filters and no data manipulation except for the described operations were used in this study. In all figures, the exact velocity values for each voxel/pixel were plotted without smoothing.

2.4 PIV reference measurements

As a reference measurement technique, Particle Image Velocimetry (PIV) was used to obtain quantitative velocity information of the flow in the venturi. The measurements were conducted in a separate experiment. However, the same flow loop as in the MRV experiment was used. All monitored flow parameters were adjusted to the same values. In contrast to the MRV experiment, in which no tracers were necessary, the flow was seeded with hollow glass particles.

These particles had a mean diameter of 12 µm and a density of 1.1 ± 0.5 g/cm^3 (Sphericell 110P8, Potter Industries). The FOV was illuminated using a laser sheet with approximately 1 mm thickness entering from the top in the x-z plane. A dual-head Nd:YAG laser (Litron Laser Ltd.) was used with a power of 100 mJ/pulse and wavelength of 532 nm. The images were acquired using a 16-bit sCMOS camera (LaVision), which was placed perpendicular to the laser sheet. The camera and laser were triggered simultaneously.

A Nikon 105 mm lens was used with a magnification of 0.29 and f-stop of 11. With these settings, the particle images cover 3–4 pixels. The laser pulse duration was set to get the average particle displacement in the range of 8–12 pixels. Furthermore, the image pair acquisition frequency was 10 Hz and for each measurement, 1000 image pairs were acquired. For the case with 2.85 L/s, a few images had cavitation bubbles in the diverging section, as this is the highest flow rate before cavitation inception. Therefore, a

continuous-time series with 140 image pairs was carefully selected, which did not contain bubbles.

A multi-pass vector evaluation was performed with interrogation window sizes of $[64 \times 64]$ and $[32 \times 32]$ pixels, respectively, both with 50% overlap; equivalent to a spatial resolution of the vector field of 0.71×0.71 mm^2. In addition, universal outlier detection was applied (Westerweel and Scarano 2005).

3 Results

3.1 Validation of PIV results

First, the accuracy of the PIV reference measurements is verified. A typical raw particle image with the vector field is shown in Fig. 3. A convergence study was conducted on the PIV data. Figure 4 shows the standard deviation σ of the difference in the mean velocities for n and $n+1$ image pairs as a function of the number of image pairs. Note that u is a matrix, which contains velocity information at all interrogation locations. The relative error reduces to 0.019% of the mean velocity after 1000 image pairs. Hence, the mean of the ensemble of 1000 pairs allows obtaining sufficient data for statistics with a minimum error from the mean.

Furthermore, from mass conservation, it is known that the flow rate through every slice (z/d location) must be constant (assuming a constant density). Any deviation would be indicative of a measurement error. As the flow is axisymmetric, the total flow rate can be determined by integrating the velocity profile radially.

Figure 5 shows the flow rates computed from the PIV data versus the flow rates measured by the flowmeter. An excellent agreement was observed except for the throat region.

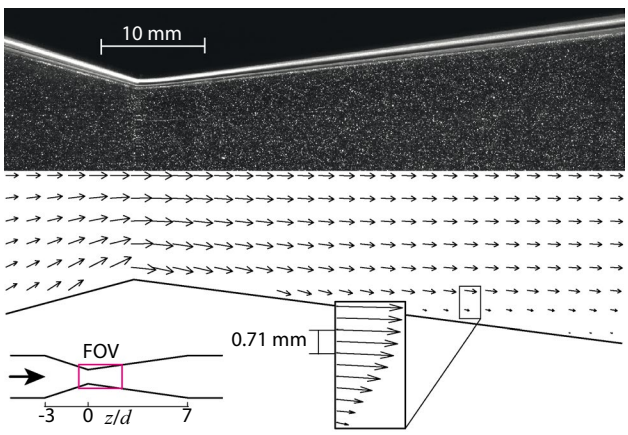

Fig. 3 (Top) typical raw particle image of the PIV acquisition. (Bottom) the resulting time-averaged vector field at the center plane. Every fifth vector is shown. The inset shows the boundary layer with the actual resolution

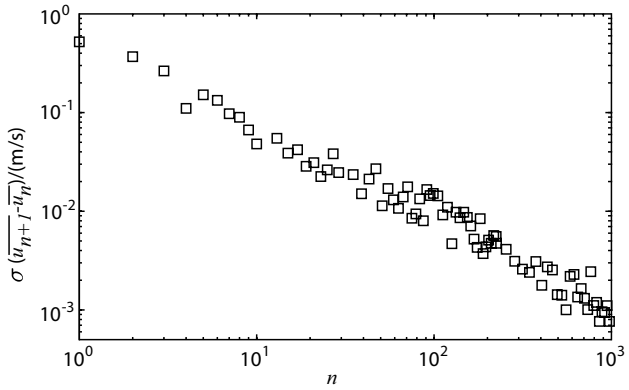

Fig. 4 Convergence study of the mean velocity field obtained with PIV. The standard deviation σ is the difference in the mean velocities for n and $n+1$ image pairs

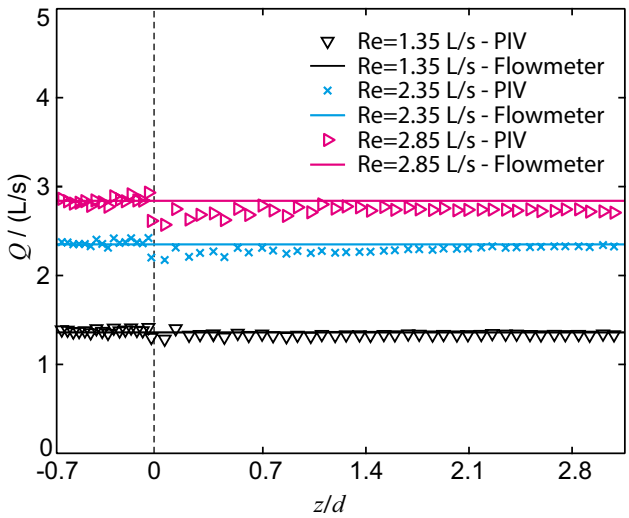

Fig. 5 Analysis of mass conservation in the PIV data by means of flow rate Q

For 2.85 L/s (Re = 71,300), the data is slightly deviating from the flowmeter reading. A maximum underestimation of 9% is observed just downstream of the venturi throat. This deviation occurs due to the presence of a high-velocity gradient at the near-wall region, which could not be resolved due to reflections from the wall. In the case of 2.85 L/s, the flow rate is slightly underestimated downstream of the throat, which might be caused by a slightly non-axisymmetric flow. Overall, the deviations are considered low, hence, the data can be used for the validation of the MRV data.

3.2 SYNC SPI versus PIV

Next, the SYNC SPI data is compared against the validated PIV data. The left column in Fig. 6 shows the qualitative

comparison of the velocity data obtained from both techniques. It is shown that the overall velocity fields match well. However, there are local deviations in the flow field near the throat of the venturi and near the channel walls. Compared to the PIV data, the velocity field at the throat appears "smeared" in the axial direction. This effect is indicated by *blue* arrows in Fig. 6.

The deviations close to the channel walls can be attributed to the relatively low resolution of the MRV data. As seen in the contour plots, the boundary between fluid and channel walls is "ragged", which has a significant effect on the shape of the boundary layer. These effects are indicated by *magenta* arrows in Fig. 6. Note that these deviations are within one voxel size of the MRV acquisition.

The velocity profiles in the right column in Fig. 6 reveal the quantitative differences in the flow field. For all flow rates, the extracted velocity profiles match well except for the local deviations identified in the contour plots. In all other flow regions, the PIV data lies within the measurement uncertainty of the MRV data (95% confidence interval equivalent to two standard deviations).

Overall, the PIV data appears "sharper" then the MRV data. Partly, this effect is related to the different slice thickness of the two measurements. The acquired MRV slice had a thickness of 5 mm, which is significantly more than the 1 mm thick laser sheet. Because of the thicker slice, the velocity field is averaged over a larger volume, which results in smoother contours. The effect of a thicker slice was assessed by synthetically sampling the PIV data onto a 5 mm thick slice. First, the top half of the PIV data was rotated by 360° assuming the flow is axisymmetric. The reconstructed three-dimensional data set was then resampled with a 5 mm thick slice and 0.75 mm in-plane resolution, which represents the measurement grid of the MRV acquisition.

Figure 7 shows the velocity profiles at the throat for both the original PIV data and the resampled PIV data in comparison to the MRV data. As expected, the peak velocity at the throat is slightly under-estimated in the resampled PIV data because of the thicker slice. Outside the peak velocity zone, the difference between the two PIV data sets decreases. In comparison, the MRV data shows a similar trend. However, the smoothing of the velocity peak is more pronounced. As a result, the deviations between MRV and PIV can be partly contributed to the thicker MRV slice. Other effects in the MRV data that may contribute to these deviations are addressed in the Discussion section.

3.3 SYNC SPI versus conventional MRV

Next, the fully sampled SYNC SPI data and the conventional MRV data are compared. Both data sets were measured on the same grid and in the same experiment. Deviations due to different experimental conditions or misalignment between the two measurement grids can, therefore, be ruled out.

Figure 8a shows the signal magnitude obtained from both MRV methods for zero flow, and the three investigated flow rates. The contour of the flow geometry is extracted from the signal magnitude via a manually set threshold. The results show that for zero flow, both MRV methods accurately reproduce the geometry of the venturi. Within the tolerance of one voxel length, the positions of the walls are depicted correctly.

For the conventional MRV data, the accuracy decreases drastically with increasing flow rate. For all investigated flow rates, the throat of the venturi is shifted downstream, which leads to remarkable distortions in the flow geometry. The shifted distance at the throat increases with higher flow rates. A maximum shift of approximately 21 mm is observed at a flow rate of 2.85 L/s. This effect can be attributed to displacement errors. No such errors are visible in the results of SYNC SPI.

Besides displacement errors, the signal magnitudes reveal other particular effects. In the cases without flow, the image magnitude of the SYNC SPI data contains more shading as compared to 4D FLOW. The reason lies in the relatively non-uniform slice profile of the SYNC SPI protocol because of low BWT, which was chosen to reduce acquisition time. For the cases with flow, the image magnitude evolves differently for the two sequence types. In the 4D FLOW data, an annular region with lower signal appears downstream of the throat, as indicated by *blue* arrows in Fig. 8a. The signal attenuation is caused by intra-voxel phase dispersion due to velocity changes within the voxels (Ehman and Felmlee 1990). The 4D FLOW data has a higher sensitivity to these effects because of lower VENC, which explains why this effect is only visible in this data.

In the case of SYNC SPI, a region of low signal is visible near the throat of the venturi, as indicated by *yellow* arrows in Fig. 8a. This effect can also be attributed to intra-voxel phase dispersion, which is, however, different from velocity dephasing. The full effects and the reason why this dephasing only occurs in the SYNC SPI data are addressed in the Discussions section.

The impact of displacement error is even more remarkable in the velocity data shown in Fig. 8b. Besides the geometrical shift, the velocity field reveals substantial distortions. As shown in the image insets, the flow develops differently downstream of the throat. While PIV and SYNC SPI data show that the boundary layer grows immediately downstream of the throat, the boundary layer in the conventional MRV data appears further downstream.

Figure 9 shows the quantitative deviations in the flow field caused by displacement errors. The velocity profiles obtained from conventional MRV exhibit substantial

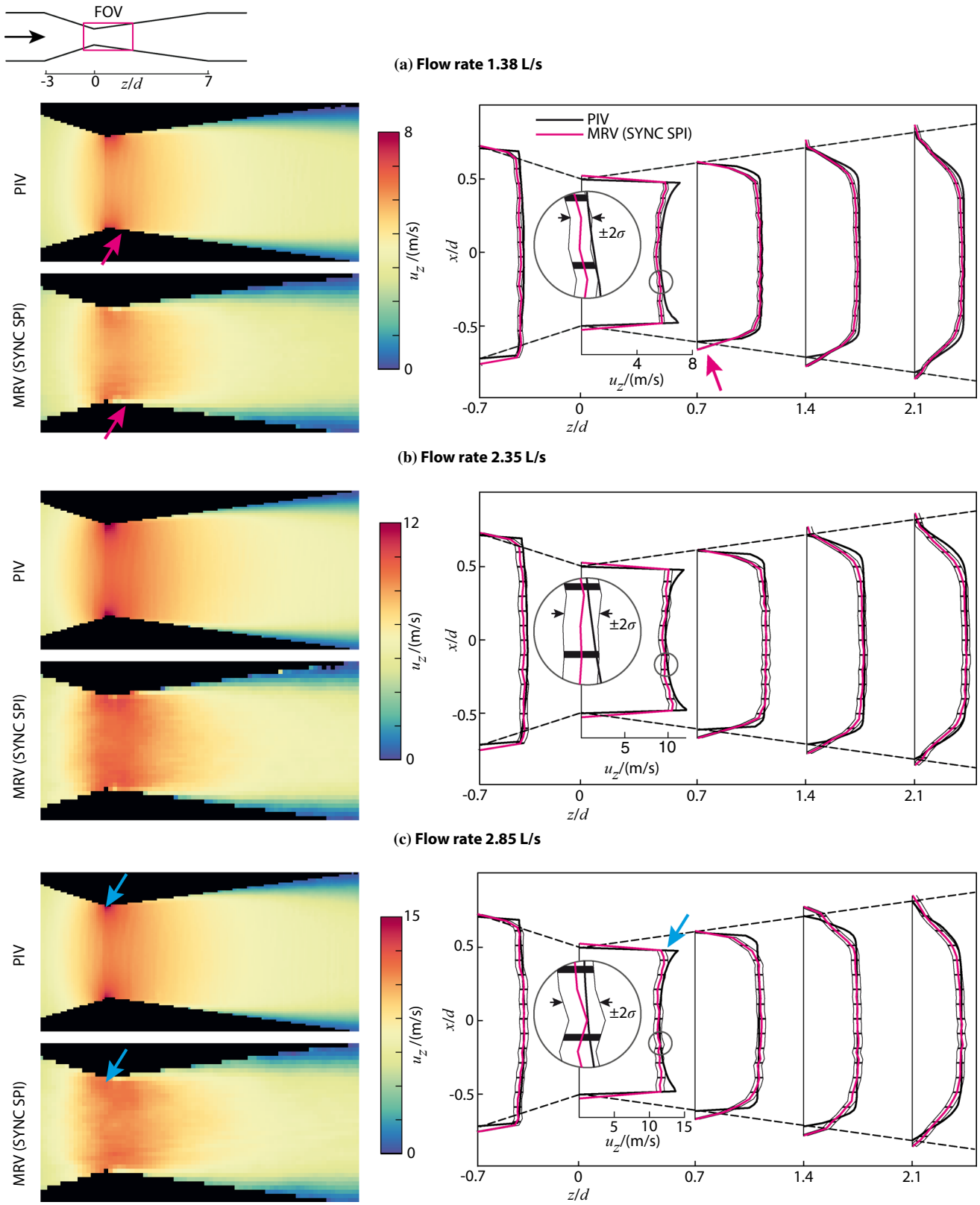
FOV
-3
0
z/d
7
(a) Flow rate 1.38 L/s
PIV
MRV (SYNC SPI)
8
0
u_z/(m/s)
PIV
MRV (SYNC SPI)
±2σ
4
8
u_z/(m/s)
x/d
0.5
0
-0.5
-0.7
0
0.7
1.4
2.1
z/d
(b) Flow rate 2.35 L/s
12
0
5
10
(c) Flow rate 2.85 L/s
15
0
5
10
15

◂**Fig. 6** Qualitative and quantitative comparison of the axial velocity fields obtained from SYNC SPI and PIV. The line plots include the measurement uncertainty of the MRV data on a 95% confidence interval, equivalent to two standard deviations (2σ). Blue arrows indicate velocity field deviations near the throat of the venturi. Magenta arrows point to velocity field deviations near the boundary layer. According to the difference approach in (Bruschewski et al. 2016a), the standard deviation of the SYNC SPI data was estimated as 0.086 m/s, 0.22 m/s, and 0.28 m/s for 1.38 L/s, 2.35 L/s, and 2.85 L/s, respectively

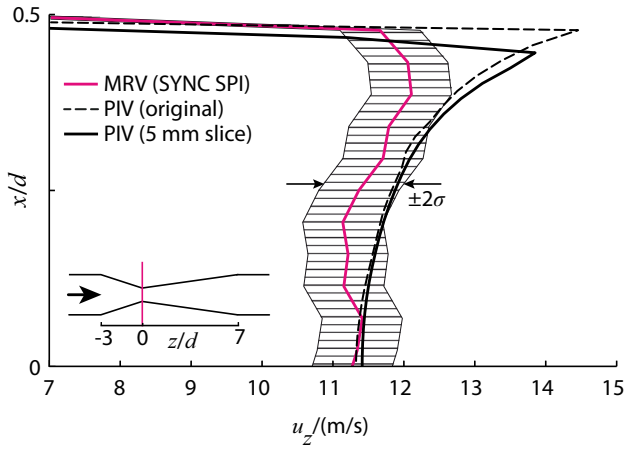

Fig. 7 Effect of the slice thickness on the velocity measurement. The original PIV data was resampled onto a 5 mm thick slice, which corresponds to the slice thickness of the MRV data

deviations. Overall, the data from conventional MRV is both qualitatively and quantitatively incorrect.

3.4 Compressed-sensed SYNC SPI versus fully sampled SYNC SPI

Finally, the effect of Compressed Sensing on measurement accuracy is investigated. As described in the methods section, the fully sampled SYNC SPI data is resampled with random undersampling masks and then non-linear reconstructed. Figure 10 shows the qualitative effect of undersampling on the signal magnitude and velocity field. It can be seen that the undersampled and zero-filled data is subject to noise-like structures in the image, which grow with a lower sampling factor. This noise is significantly reduced in the non-linear reconstructed data. For all sampling factors, no significant deviations between fully sampled and non-linear reconstructed velocity data are visible.

Figure 11 shows the quantitative comparison between the fully sampled, zero-filled, and non-linear reconstructed velocity data. The zero-filled data is considerably noisier than the fully sampled data. However, systematic velocity deviations are not visible. After non-linear reconstruction, most of the noise disappears, and the reconstructed velocity profiles match closer to the fully sampled data.

Some local deviations between the fully sampled and non-linear reconstructed data are visible for low sampling factors. Some flow features such as the "W-shaped" velocity profile at the throat appear slightly different. For a sampling factor of 30% and more, almost all deviations are within the measurement uncertainty of the fully sampled data on a 95% confidence interval.

4 Discussion

4.1 Displacement errors in conventional MRV

In the presented measurements, an MRV sequence based on the 4D FLOW technique produced strong displacement errors for all investigated flow rates. A maximum displacement of 21 mm was observed for a flow velocity of approximately 12 m/s. Note that these effects were not exaggerated on purpose. The applied conventional MRV sequence was optimized for the shortest possible TE at the present MRI hardware.

In Table 1, the degree of displacement was estimated based on the encoding delay and TE as a representative time scale. The same calculation was applied to the 4D FLOW measurements in this study. The results are presented in Table 3. The estimator based on the encoding delay (Eq. (1)) yields accurate displacement values. Note that all estimated values are slightly larger than the measured values. The reason for the overestimation is that this estimator considers the maximum velocity at the throat, while in the measurement, the moving fluid also experiences lower velocity zones during spatial encoding. As a result, Eq. (1) can be regarded as robust and conservative. The estimation based on TE (Eq. (2)) produces consistently higher displacement values, which was expected because TE is always longer than the actual encoding delay. However, this estimator is still useful in cases in which the exact encoding delay is not known.

An accurate estimation of the displacement error helps in evaluating whether a sequence can be used for a specific flow measurement. In many cases, a moderate degree of displacement errors needs to be tolerated, especially at MRI facilities where scanner time is limited. Therefore, conventional MRV based on the 4D FLOW sequence still plays an important role as an efficient flow measurement technique.

4.2 Residual errors in the SYNC SPI data

SYNC SPI was found less prone to displacement errors. The comparison with PIV showed a sufficient agreement of the flow field results. However, some regions in the flow field could be identified, in which SYNC SPI produced local velocity errors or reduced SNR. Following measurement errors were identified that may contribute to these effects:

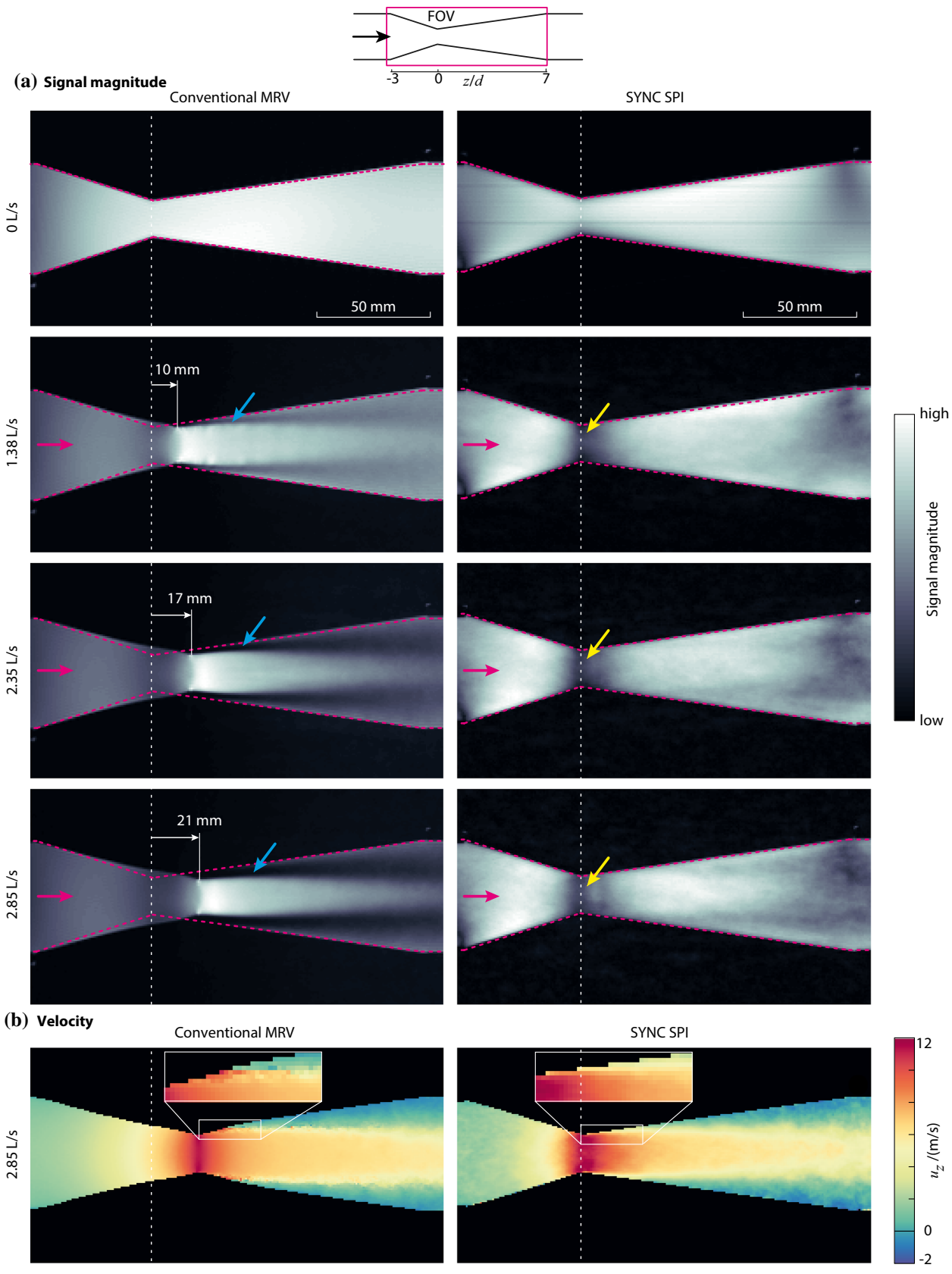
FOV
-3
0
z/d
7
(a) Signal magnitude
Conventional MRV
SYNC SPI
0 L/s
1.38 L/s
2.35 L/s
2.85 L/s
50 mm
50 mm
10 mm
17 mm
21 mm
high
Signal magnitude
low
(b) Velocity
Conventional MRV
SYNC SPI
2.85 L/s
12
u_z /(m/s)
0
-2

◂**Fig. 8** Qualitative comparison of the signal magnitude (**a**) and axial velocity field (**b**) corresponding to conventional MRV and SYNC SPI. Magenta arrows indicate the mean flow direction. Magenta dashed lines indicate the actual geometry of the venturi. White dashed lines mark the actual location of the throat of the venturi. The position of the geometry in the images was obtained by fitting the signal magnitude of the zero-flow data onto the original geometry. Blue and yellow arrows indicate regions of motion-induced signal loss. Segmentation from the background is performed for the velocity fields using the associated signal magnitudes. The image insets in **b** show the flow development downstream of the throat

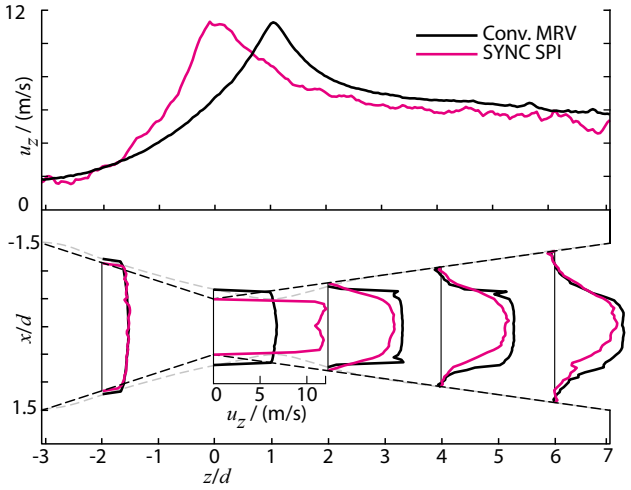

Fig. 9 Quantitative comparison of the axial velocity data corresponding to conventional MRV and SYNC SPI for the flow rate (2.85 L/s). The black and gray dashed lines indicate the contours of the venturi extracted from the SYNC SPI and conventional MRV data, respectively

- *Residual displacement errors* As described in the Introduction section, inter-encoding misregistration errors can be removed by synchronizing all encoding gradients. This is the case in SYNC SPI. However, intra-encoding misregistration errors can never be completely removed because the encoding gradients always have a finite duration. The effect of intra-encoding misregistration can be described as a smoothing process. Velocity peaks appear less distinct since the velocity data is "smeared" in the stream-wise direction. This effect is visible near the throat of the venturi in Fig. 6. The velocity peak at the throat is less distinct compared to the PIV data. In comparison to conventional 4D FLOW, the effect of velocity smearing is relatively strong. The reason lies in the particular velocity encoding process of SYNC SPI. As seen in Fig. 1b, the lobes of the bipolar velocity encoding gradients are separated to achieve perfect synchronization of all encoding events, and therefore remove inter-encoding misregistration. However, the velocity encoding duration is made longer, which causes stronger velocity smearing.
- *Velocity errors related to higher orders of motion* The velocity acquisition in MRV is based on the assumption that the velocity of the fluid is constant during velocity encoding. This assumption is not valid in flows with acceleration and jerk, which are the second and third derivative of motion. Because of the relatively long velocity encoding duration in SYNC SPI, the phase of the signal is particularly sensitive to these effects. The phase changes caused by higher orders of motion are misinterpreted as velocity, which may explain some of the local velocity errors.
- *Motion artifacts caused by flow turbulence* In addition to systematic errors, the effect of random errors requires attention. In general, flow turbulence and other transient effects cause signal ghosts along with all phase-encoding directions. Since SYNC SPI is a purely phase-encoded technique, these signal ghosts appear as elevated noise in the entire image. Note that with conventional sequences such as 4D FLOW, these signal ghosts do not appear along the frequency-encoding direction. As a result, SYNC SPI is more prone to motion artifacts compared to imaging methods with frequency encoding such as 4D FLOW.
- *Signal attenuation related to motion* In general, any non-uniform motion within a voxel leads to phase dispersion and, therefore, to signal attenuation. It depends on the motion sensitivity of the encoding process, whether these effects are significant. The signal dephasing caused by changes in velocity depends directly on the parameter VENC. This parameter is a design parameter of the sequence, and the signal attenuation related to VENC can be controlled. However, higher orders of motion, such as acceleration and jerk may have a similar effect. In Fig. 6, it can be seen that the SYNC SPI data has a low-signal area at the throat. This area coincides with a region with a particularly strong change in acceleration and jerk. Intra-voxel phase dispersion caused by this change in motion leads to the observed signal attenuation. The 4D FLOW data is less affected because the velocity encoding process is shorter and, therefore, less sensitive to phase dispersion caused by higher orders of motion.

In summary, SYNC SPI resolves inter-encoding misregistration at the price of longer acquisition time, increased velocity smoothing, and locally as well as globally decreased SNR. These effects are inherent to the encoding process of SYNC SPI. As a remedy, the duration of the velocity encoding event must be decreased, which can be accomplished by faster switching hardware or optimized sequence structure. Furthermore, a large number of averages might be necessary to achieve a sufficient SNR level in the entire image, which further prolongs the acquisition time.

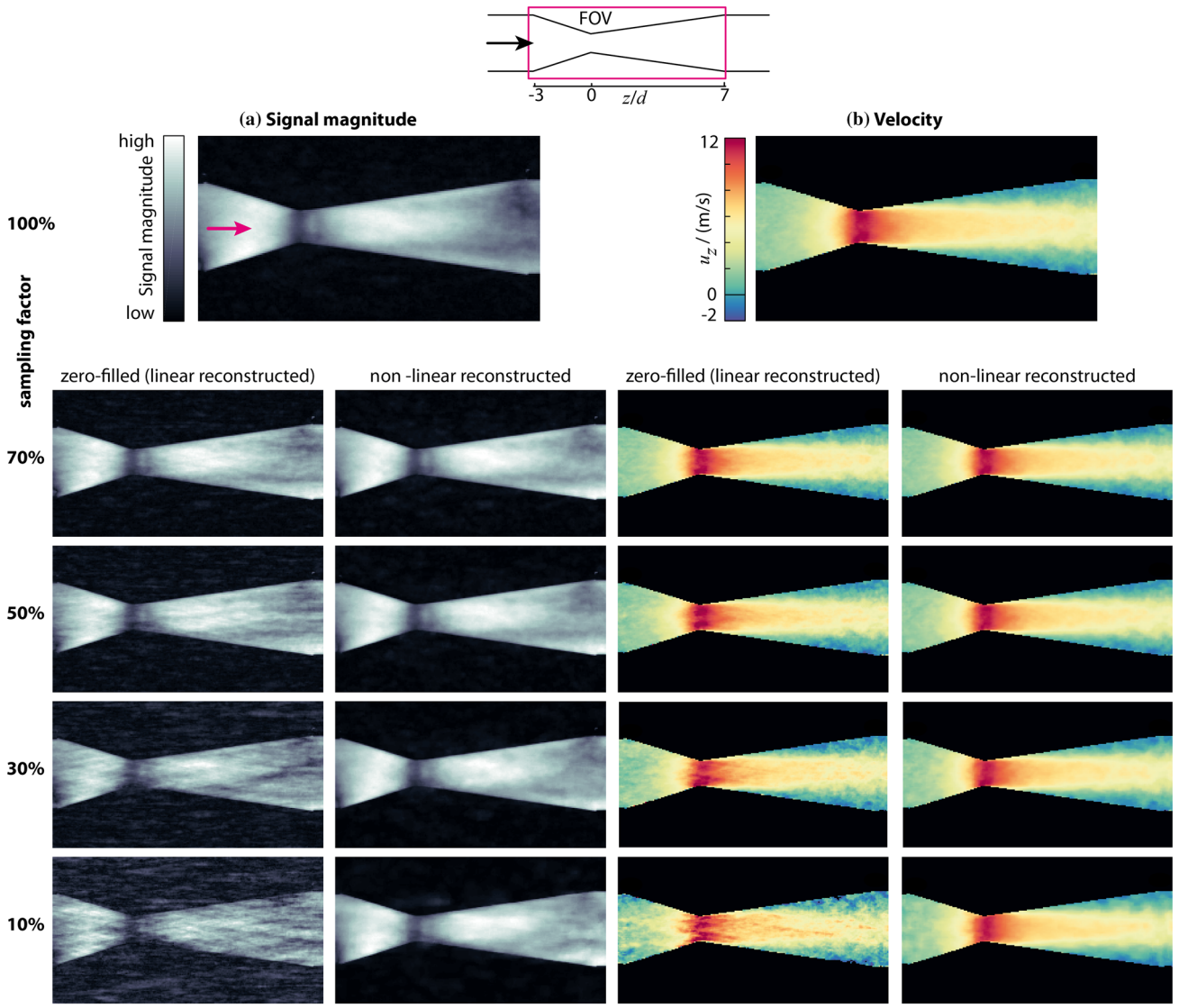

Fig. 10 Qualitative comparison of the signal magnitude and axial velocity field corresponding to fully sampled SYNC SPI, zero-filled SYNC SPI, and non-linear reconstructed SYNC SPI. Magnitude images are not segmented. Velocity images are segmented using the signal magnitude of the fully sampled data

4.3 Advantages of compressed sensing in SYNC SPI

As the acquisition time has been so far the most significant disadvantage of SYNC SPI, the most remarkable result to emerge from this study is the application of Compressed Sensing. The velocity data reconstructed from undersampled data were in good agreement to the fully sampled cases. Noticeable deviations caused by undersampling started to appear at the lowest investigated sampling factor of 10%. At a sampling factor of 30% and higher, almost all velocity deviations are within the measurement uncertainty of the fully sampled data (95% confidence interval).

The possibility to reduce the measured data by up to 70% translates directly in a 70% reduction in acquisition time. In this example, the acquisition time was reduced from 220 to 66 s. Note that the computing time for the non-linear reconstruction is considerably longer than for conventional image reconstruction. However, this is to put in perspective as computing time is better accessible and cheaper than MRI measurement time.

In this study, iterative reconstruction for each velocity map was conducted in less than a minute with a single-threaded process on a standard desktop computer. However, this time can be significantly decreased by parallel computing. Untenberger et al. (2016) demonstrate that a similar reconstruction can be achieved in less than 100 milliseconds using multiple graphical processing units.

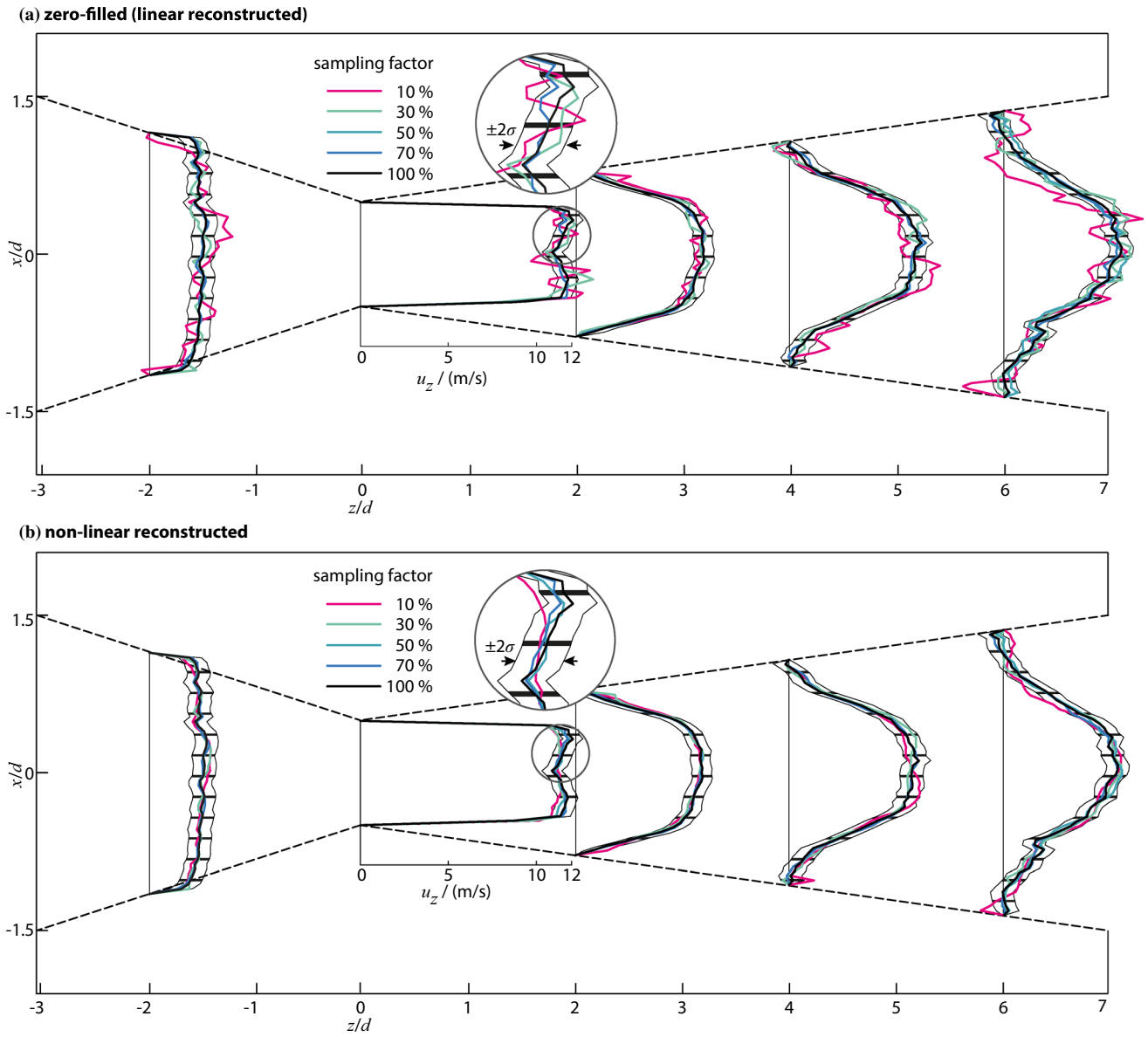

Fig. 11 Quantitative comparison of the axial velocity profiles corresponding to fully sampled SYNC SPI, zero-filled SYNC SPI, and non-linear reconstructed SYNC SPI. The tolerance band corresponds to the measurement uncertainty (95% confidence interval) of the fully sampled data

Table 3 Evaluation of Eqs. (1) and (2) for the investigated flows and comparison to the measured displacement values

Flow case (L/s)	Measured displacement (number of voxels)	Estimation based on encoding delay (number of voxels)	Estimation based on TE (number of voxels)
1.38	13	15	22
2.35	23	26	36
2.85	28	32	43

Choosing the right undersampling factor is the greatest challenge in the application of Compressed Sensing. In contrast to this study, the fully sampled data, or another ground truth, is typically not available in actual flow experiments. The lowest suitable sampling factor may depend on the complexity of the geometry and flow field as well as on the SNR level of the measurements.

A suitable sampling factor can be chosen from experience or simulation. As one of many possible ways, we propose the following approach. The flow data is first acquired with

a quick MRV acquisition, for example, using a 4D FLOW sequence. Although this data contains displacement errors, the measured geometry and the flow field are representative of the image reconstruction process. This data is then synthetically undersampled with various sampling factors until a suitable number is found. Finally, the SYNC SPI is undersampled using the sampling mask that was determined in these simulations.

5 Conclusion

This study focused on the measurement accuracy of MRV. It was demonstrated that displacement errors always occur in the data obtained with MRV sequences based on the 4D FLOW technique. Displacement errors are particularly crucial in experiments with high flow velocities and high spatial resolution. Depending on the measured flow system, these errors might not be directly visible in the results but they always occur. Neglecting the effect of displacement in flow acquisitions may results in severe misinterpretation of the results. In many cases, a sequence similar to SYNC SPI is required to achieve sufficient measurement accuracy.

Supported by PIV data, this study highlighted the reliability of SYNC SPI to acquire accurate mean velocity data in turbulent high-speed flows. In comparison to the 4D FLOW technique, the acquisition time of SYNC SPI is orders of magnitude longer. For this reason, it is beneficial to implement an imaging acceleration technique such as Compressed Sensing. With this technique, the acquisition time could be decreased by up to 70% while maintaining the same resolution and a similarly high measurement accuracy.

It is stressed that, despite the reduction in acquisition time, the SYNC SPI technique is not capable of providing time-resolved data at reasonable frame rates. In this example, a 70% reduction in acquisition time resulted in 66 s remaining time. However, time-resolved measurements were not the objective in designing the SYNC SPI sequence.

In conclusion, SYNC SPI proves to be a reliable method for measurements in high-speed turbulent flows. This new technique is particularly valuable for laboratory experiments where mean flow velocities are to be measured at high accuracy. Because of the point-wise *k*-space sampling, imaging acceleration techniques such as Compressed Sensing can be easily implemented to make the data acquisition more efficient.

References

Baek S, Lee S, Hwang W, Park JS (2019) Experimental and numerical investigation of the flow in a trailing edge ribbed internal cooling passage. J Turbomach 141(1):011–012

Bernstein MA, Shimakawa A, Pelc NJ (1992) Minimizing TE in moment-nulled or flow-encoded two-and three-dimensional gradient-echo imaging. J Magn Reson Imaging 2(5):583–588

Bruschewski M, Freudenhammer D, Buchenberg WB, Schiffer HP, Grundmann S (2016a) Estimation of the measurement uncertainty in magnetic resonance velocimetry based on statistical models. Exp Fluids 57(5):83

Bruschewski M, Scherhag C, Schiffer HP, Grundmann S (2016b) Influence of channel geometry and flow variables on cyclone cooling of turbine blades. J Turbomach 138(6):061,005–061,005

Bruschewski M, Kolkmannn H, John K, Grundmann S (2019) Phase-contrast single-point imaging with synchronized encoding: a more reliable technique for in vitro flow quantification. Magn Reson Med 81(5):2937–2946

Candes EJ, Romberg JK, Tao T (2006) Stable signal recovery from incomplete and inaccurate measurements. Commun Pure Appl Math J Issued Courant Inst Math Sci 59(8):1207–1223

Ching DS, Elkins CJ, Eaton JK (2018) Investigation of geometric sensitivity of a non-axisymmetric bump: 3d mean velocity measurements. Exp Fluids 59(9):143

Donoho DL et al (2006) Compressed sensing. IEEE Trans Inf Theory 52(4):1289–1306

Ehman RL, Felmlee JP (1990) Flow artifact reduction in MRI: a review of the roles of gradient moment nulling and spatial presaturation. Magn Reson Med 14(2):293–307

Elkins CJ, Alley MT (2007) Magnetic resonance velocimetry: applications of magnetic resonance imaging in the measurement of fluid motion. Exp Fluids 43(6):823–858

Elkins CJ, Alley MT, Saetran L, Eaton JK (2009) Three-dimensional magnetic resonance velocimetry measurements of turbulence quantities in complex flow. Exp Fluids 46(2):285–296

Freudenhammer D, Baum E, Peterson B, Böhm B, Jung B, Grundmann S (2014) Volumetric intake flow measurements of an IC engine using magnetic resonance velocimetry. Exp Fluids 55(5):1724

Grundmann S, Wassermann F, Lorenz R, Jung B, Tropea C (2012) Experimental investigation of helical structures in swirling flows. Int J Heat Fluid Flow 37:51–63

Holland DJ, Malioutov DM, Blake A, Sederman AJ, Gladden L (2010) Reducing data acquisition times in phase-encoded velocity imaging using compressed sensing. J Magn Reson 203(2):236–246

Jahangir S, Hogendoorn W, Poelma C (2018) Dynamics of partial cavitation in an axisymmetric converging–diverging nozzle. Int J Multiph Flow 106:34–45

Larson T 3rd, Kelly W, Ehman RL, Wehrli F (1990) Spatial misregistration of vascular flow during MR imaging of the CNS: cause and clinical significance. Am J Roentgenol 155(5):1117–1124

Layton KJ, Kroboth S, Jia F, Littin S, Yu H, Leupold J, Nielsen JF, Stöcker T, Zaitsev M (2017) Pulseq: a rapid and hardware-independent pulse sequence prototyping framework. Magn Reson Med 77(4):1544–1552

Lustig M, Donoho D, Pauly JM (2007) Sparse MRI: the application of compressed sensing for rapid MR imaging. Magn Reson Med 58(6):1182–1195

Lustig M, Donoho DL, Santos JM, Pauly JM (2008) Compressed sensing MRI. IEEE Signal Process Mag 25(2):72

Markl M, Frydrychowicz A, Kozerke S, Hope M, Wieben O (2012) 4D flow MRI. J Magn Reson Imaging 36(5):1015–1036

Nishimura DG, Jackson JI, Pauly JM (1991) On the nature and reduction of the displacement artifact in flow images. Magn Reson Med 22(2):481–492

Onstad AJ, Elkins CJ, Medina F, Wicker RB, Eaton JK (2011) Full-field measurements of flow through a scaled metal foam replica. Exp Fluids 50(6):1571–1585

Piro M, Wassermann F, Grundmann S, Leitch B, Tropea C (2016) Progress in on-going experimental and computational fluid dynamic investigations within a CANDU fuel channel. Nucl Eng Des 299:184–200

Untenberger M, Tan Z, Voit D, Joseph AA, Roeloffs V, Merboldt KD, Schätz S, Frahm J (2016) Advances in real-time phase-contrast flow MRI using asymmetric radial gradient echoes. Magn Reson Med 75(5):1901–1908

Wapler MC, Leupold J, Dragonu I, von Elverfeld D, Zaitsev M, Wallrabe U (2014) Magnetic properties of materials for MR engineering, micro-MR and beyond. J Magn Reson 242:233–242

Wassermann F, Hecker D, Jung B, Markl M, Seifert A, Grundmann S (2013) Phase-locked 3D3C-MRV measurements in a bi-stable fluidic oscillator. Exp Fluids 54(3):1487

Westerweel J, Scarano F (2005) Universal outlier detection for PIV data. Exp Fluids 39(6):1096–1100